An Estimation of the Climatic Effects of Stratospheric Ozone Losses during the 1980s

ROBERT M. MACKAY, MALCOLM K. W. KO, RUN-LIE SHIA, AND YAJAING YANG

Atmospheric and Environmental Research, Inc., Cambridge, Massachusetts

SHUNTAI ZHOU

National Centers for Environmental Prediction, Washington, D.C.

GYULA MOLNAR

NASA/Goddard Space Flight Center, Greenbelt, Maryland

(Manuscript received 22 January 1996, in final form 11 September 1996)

ABSTRACT

In order to study the potential climatic effects of the ozone hole more directly and to assess the validity of previous lower resolution model results, the latest high spatial resolution version of the Atmospheric and Environmental Research, Inc., seasonal radiative dynamical climate model is used to simulate the climatic effects of ozone changes relative to the other greenhouse gases. The steady-state climatic effect of a sustained decrease in lower stratospheric ozone, similar in magnitude to the observed 1979–90 decrease, is estimated by comparing three steady-state climate simulations: I) 1979 greenhouse gas concentrations and 1979 ozone, II) 1990 greenhouse gas concentrations with 1979 ozone, and III) 1990 greenhouse gas concentrations with 1990 ozone. The simulated increase in surface air temperature resulting from nonozone greenhouse gases is 0.272 K. When changes in lower stratospheric ozone are included, the greenhouse warming is 0.165 K, which is approximately 39% lower than when ozone is fixed at the 1979 concentrations. Ozone perturbations at high latitudes result in a cooling of the surface–troposphere system that is greater (by a factor of 2.8) than that estimated from the change in radiative forcing resulting from ozone depletion and the model's $2 \times CO_2$ climate sensitivity. The results suggest that changes in meridional heat transport from low to high latitudes combined with the decrease in the infrared opacity of the lower stratosphere are very important in determining the steady-state response to high latitude ozone losses. The 39% compensation in greenhouse warming resulting from lower stratospheric ozone losses is also larger than the 28% compensation simulated previously by the lower resolution model. The higher resolution model is able to resolve the high latitude features of the assumed ozone perturbation, which are important in determining the overall climate sensitivity to these perturbations.

1. Introduction

Assessing the climatic effects of changes in atmospheric trace gas concentrations is an important scientific issue as well as an essential component of social, economic, and political policy development. The major atmospheric greenhouse gases (H_2O, CO_2, CH_4, O_3, N_2O, CFC-11, and CFC-12) absorb infrared radiation emanating from the earth's surface and reradiate part of this energy back to the surface. This greenhouse ''trapping,'' coupled with the fact that these greenhouse gases absorb a relatively small fraction of the incident solar radiation, results in the earth's surface being warmer than it would be without these gases present in the atmosphere. Since ozone is also a strong absorber of solar radiation, the climatic effects of ozone perturbations are more complex than for the other greenhouse gases. In this work we use a two-dimensional climate model to better understand the climatic effects of ozone perturbations.

Observations over the last ten to twenty years indicate that ozone concentrations in the lower stratosphere have decreased and that tropospheric ozone concentrations have possibly increased in some regions (e.g., see Stolarski et al. 1991; McCormick et al. 1992; Logan 1994). Since ozone is a strong absorber of both solar and terrestrial radiation, these ozone changes can affect the radiation budget of the surface–troposphere system in several ways: 1) Decreases in stratospheric ozone concentrations result in reduced solar absorption by the stratosphere. Hence, more solar energy reaches the surface–troposphere system (tropospheric warming); 2) Decreases in stratospheric ozone reduce the thermal emissivity of the stratosphere, and, hence, less infrared radiation reaches the troposphere (tropospheric cooling); 3) Lower ozone concentrations in the stratosphere

Corresponding author address: Dr. Robert M. MacKay, Clark College, 1800 E. McLoughlin Blvd., Vancouver, WA 98663-3598

© 1997 American Meteorological Society

Unauthenticated | Downloaded 10/21/21 05:38 AM UTC

also tend to make the stratosphere cooler (less solar absorption by the stratosphere) and hence less thermal energy will be radiated by the stratosphere downward into the troposphere (tropospheric cooling); and 4) Increases in tropospheric ozone will result in an increased greenhouse trapping of longwave radiation (tropospheric warming). It is not immediately clear which of the above effects is strongest. Since the observational evidence for changes in tropospheric ozone are highly variable and presently inconclusive (e.g., see Logan 1994), we do not attempt to address the climatic effects of the observed changes in tropospheric ozone here.

Ramanathan and Dickinson (1979), Wang and Sze (1980), and Lacis et al. (1990) have stressed the importance of the vertical distribution of ozone changes to the net radiative forcing of the surface–troposphere system. Using a one-dimensional radiative–convective model (1D RCM), Lacis et al. found that 1) ozone depletion below about 30 km resulted in a net cooling of the earth's surface and 2) the surface temperature is most sensitive to changes in ozone that occur near the tropopause. These conclusions are in general agreement with the results of others.

Ramaswamy et al. (1992) used observed 1979–90 ozone losses and measured increases in the other greenhouse gases over the same time period to estimate the net radiative adjusted forcing of the troposphere during the 1980s.[1] They compared this radiative forcing to that calculated with ozone held fixed and found that the assumed ozone depletion in the lower stratosphere reduced the net radiative forcing at the tropopause. Schwarzkopf and Ramaswamy (1993) explored the sensitivity of the above radiative forcing to the assumed vertical profile of ozone changes and also found that their results were particularly sensitive to the assumed changes in stratospheric ozone near the tropopause. Since the Total Ozone Mapping Spectrometer (TOMS) measures total column ozone and the Stratospheric Aerosol and Gas Experiment (SAGE) measures ozone down to about 17 km, the actual ozone profile in the layer between the tropopause and 17 km is highly uncertain. This results in correspondingly large uncertainties in the actual radiative forcing of the surface–troposphere system, particularly at high latitudes where the tropopause is lowest.

In addition to stressing the importance of the vertical and latitudinal variations in ozone changes, Molnar et al. (1994, hereafter M94) have emphasized the importance of seasonal variations in percent ozone changes to the resulting net radiative forcing. They have also noted that although it is often assumed that the surface temperature response is linearly related to the net radiative forcing in 1D RCMs, this is a poor assumption for higher-dimensional climate models, or for the real climate system, which include nonlinear feedback processes. Ramanathan and Dickinson (1979) note that perturbations in solar radiation (due to ozone changes) most strongly influence the surface heating and perturbations of longwave radiation strongly influence the heating of the upper troposphere. This redistribution of heating rates adds to the complexity of estimating changes in surface air temperature from net radiative forcing of the troposphere. To avoid the problems associated with using radiative forcing as a proxy for climate change, Molnar et al. used the three-zone AER seasonal radiative–dynamical (ASRD) model to investigate the steady-state response of the surface–troposphere system to sustained 1979–90 greenhouse gas changes with and without variations in lower-stratospheric ozone. In M94 the seasonal and latitudinal variations of total column ozone changes from 1979 to 1990 were estimated from TOMS.

The three-zone ASRD used in M94 divided the earth into three latitude zones 90°–30°N (northern extratropics), 30°N–30°S (Tropics), and 30°–90°S (southern extratropics) and hence, had limited horizontal resolution. Here we follow the study of M94 using the newest version of the ASRD, which has a much higher horizontal resolution (19 latitude zones each of approximately 9.5°). Since the percent changes in column ozone are greatest at high latitudes, our hypothesis is that this increased latitudinal resolution will provide additional insights into ozone's influence on the climate system than were possible with the three-zone model of M94.

The remainder of this paper is outlined as follows. In section 2 the 19-zone ASRD (ASRD-19) model is described. To provide an indication of the model's performance, the sensitivity of the model to a doubling of carbon dioxide is discussed in section 3. In section 4 we compare the 1979–90 steady-state greenhouse warming simulated by the model for two cases: 1) with the atmospheric ozone field held fixed and 2) when ozone concentrations in the lower stratosphere are reduced by an amount based on TOMS observations for this time period (identical to that used by M94). We summarize our results in section 5.

2. The climate model

The climate model is a refined version of the AER seasonal radiative–dynamical climate model (Wang et al. 1990; M94) with higher meridional resolution (19 latitude zones, ASRD-19, versus 3). The ASRD-19 is a global energy balance model that computes the seasonal 2D temperature field from the radiative and dynamical heat balance of the atmosphere and subsurface layer. The atmosphere is divided into eight vertical layers in the stratosphere and ten layers in the troposphere. It includes 19 latitudinal zones from pole to pole, each approximately 9.47° in width. Separate land and ocean sectors are included within each latitudinal zone, and the heat exchange between the land and ocean sectors is computed according to a turbulent diffusion law with

[1] See IPCC (1994) and Molnar et al. (1994) for definitions and discussion of initial and adjusted radiative forcing. We discuss the specifics of our method further in section 4.

Unauthenticated | Downloaded 10/21/21 05:38 AM UTC

empirical diffusion coefficients. The simulations of ice and snow albedo are the same as in M94 except that snow-free land albedos are taken from Hansen et al. (1983). Ice-free ocean albedos are estimated as in Briegleb et al. (1986). The albedo for direct solar radiation is dependent on the solar zenith angle and for diffuse radiation is assumed to be 0.06.

Radiative transfer calculations are performed as in M94. The solar radiation scheme used in the model is based on Lacis and Hansen (1974) except that the improved frequency integration scheme described by Wang and Ryan (1983) is used to calculate the total solar flux. Seasonal variations in solar intensity reaching the top of the atmosphere due to the earth's eccentricity are also included. The thermal radiation parameterization is based on the correlated k-distribution method described by Wang and Ryan (1983). This method allows a rigorous treatment of coupled radiative processes of absorption and multiple scattering due to gases and particles in an inhomogeneous atmosphere. Twenty-seven narrow spectral intervals are used to account for the nongray gaseous absorption of H_2O, CO_2, O_3, N_2O, CH_4, and CFCs and the spectral properties of clouds, especially for high cirrus.

Seasonally varying cloud amounts, relative humidity, and ozone are all prescribed in the model based on observations. The primary differences between the ASRD-19 and the three-zone version described by M94 are outlined below.

a. Oceanic meridional heat transport

The meridional heat transfer in the mixed layer ocean is calculated assuming that the turbulent diffusion of ocean heat energy is directly proportional to the meridional gradient of mixed layer temperature. Using the notation of Watts and Morantine (1990), the temperature change of the mixed layer ocean is calculated from

$$\frac{\partial T_o}{\partial t} = \frac{K_H}{(1 - f_i H_i/D) f_o R^2} \frac{1}{\cos\phi} \frac{\partial}{\partial \phi}\left(\cos\phi \frac{\partial T_o}{\partial \phi}\right) + \frac{(S + \mathrm{IR} - \mathrm{LH} - \mathrm{SH})(1 - f_i) + F_B}{(1 - f_i H_i/D)\rho C_w D}, \quad (1)$$

where T_o is the mixed layer temperature, K_H the horizontal thermal diffusivity, R the radius of the earth, and ϕ is the latitude in radians; $S+\mathrm{IR}$ is the net flux of solar plus terrestrial radiation into the ocean, LH and SH are the latent and sensible heat fluxes from the ocean surface, ρ is the density of water (taken as 1000 kg m^{-3}), C_w the specific heat capacity of water (4186 J $kg^{-1}K^{-1}$), D is the mixed layer depth (50 m), H_i is the sea ice thickness, and F_B is the rate of energy exchange (W m^{-2}) between the ocean and sea ice. The term f_o, which is implicitly assumed to be unity in the study of Watts and Morantine, is the zonal fraction of ocean in a latitude belt, and f_i is the fraction of ocean that is covered by sea ice. We use constant values of $K_H = 1.6 \times 10^{12}$ m^2 yr^{-1} and 2.1×10^{12} m^2 yr^{-1} for the Northern and Southern Hemispheres, respectively. These are comparable to the value of 1.2×10^{12} m^2 yr^{-1} used by Watts and Morantine and were adjusted to give a good simulation of observed ice cover and ocean temperature in each hemisphere. The thermodynamic sea ice model used is that described by M94 except that here ocean heat fluxes are calculated as described above instead of using the ''q-flux'' flux adjustment method described in M94. Thus, the present model has a fully prognostic determination of sea ice.

b. Atmospheric meridional heat transport

Meridional heat transport by the atmosphere in the middle to high latitudes is dominated by large-scale eddies. In this work we assume that the stratosphere is heated by radiant energy only and that all atmospheric meridional heat transport is confined to the troposphere. Shine (1987) explored the radiative steady state of the stratosphere to seasonally variable solar radiation and showed that temperature reductions during polar night depended on the thermal response time of the stratosphere. Accordingly, the thermal response time of our model stratosphere has been increased to prevent stratospheric temperatures from falling drastically during polar night. There have been a variety of parameterization schemes for tropospheric eddy heat transport in the literature, which are based on baroclinic theory. Here we adopt the scheme developed by Stone (1974) and modified by Peng et al. (1982). It is based in part on the Eady (1949) model and in part on the two-layer model (Holton 1979).

Meridional heat transport in the Tropics is dominated by the Hadley cell transport. Unfortunately, the theoretical basis for the parameterization of Hadley cell heat transport is weak and the empirical correlation between heat transport and temperature gradient is poor. The only practical scheme for an energy balance model is that developed by Peng et al. (1987). This parameterization scheme is based on the theoretical results of Held and Hou (1980) and the empirical study of Rennick (1977). We use the Peng et al. scheme in our model as a framework and make some modifications to the vertical distribution of heat transport. Peng et al. calculated the total heat transport first, then its distribution to each layer according to an empirical relation, which is a third-order polynomial of surface temperature, multiplied by the surface adiabatic lapse rate. In order to be consistent with the parameterization schemes for vertical heat transport in our model, we do not use this empirical relation. Instead, we use the moist adjustment described below, which gives a good simulation of the atmosphere's vertical structure.

Figure 1 compares the observational estimates of the annual average meridional heat fluxes with those simulated by the model control run (described below) for

Unauthenticated | Downloaded 10/21/21 05:38 AM UTC

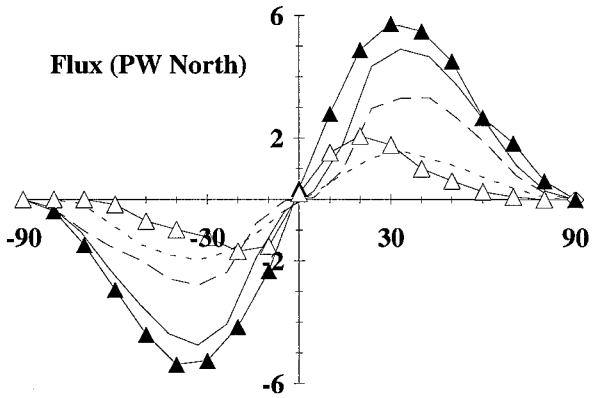

FIG. 1. Model simulated meridional heat transport in oceans (short dash), atmosphere (long dash), and total (atmosphere plus oceans: solid) compared with observed values given by Piexoto and Oort (1992) for total transport (solid triangles) and oceanic transport [Trenberth and Solomon (1994): open triangles] [Units are 10^{15} watts (PW)].

the atmosphere, total, and ocean (total minus atmosphere). The model simulates the magnitude and distribution of the total meridional heat flux reasonably well; that is, peak fluxes at mid latitudes agree to within about 15% of observations. The difference between the simulated and observed meridional heat fluxes is largest for the ocean component. The simulated peak poleward oceanic heat transport is shifted poleward by 10°–15° degrees relative to that of the observations in both hemispheres. Trenberth and Solomon (1994) quoted an estimate of the uncertainty in total oceanic heat transport of ± 0.45 PW for 45°N. Our simulated oceanic heat transport does fall within this range of observation for this location. Reducing the large differences between the simulated and observed oceanic meridional heat transports will require improvements beyond the parameterization described by (1).

c. Vertical heat transport in the atmosphere

The lapse rate adjustment scheme of Stone and Carlson (1979) has been modified slightly to improve the model's simulation of temperatures in the tropical troposphere. Vertical heat transport is implicitly included by using the baroclinic adjustment scheme for middle to high latitudes and a moist lapse rate adjustment in the Tropics. The moist adiabatic lapse rate γ_m at the surface is used to calculate $\partial\theta/\partial p|_{z=0}$ (the rate of change of potential temperature θ with respect to pressure p at the surface) using

$$\frac{\partial\theta}{\partial p} = \frac{0.288\theta}{p}\left(\frac{\gamma_m}{\gamma_d} - 1\right) \tag{2}$$

[see Houghton (1986) for a derivation of (2)]. The critical lapse rate γ_c at other vertical levels is then calculated by assuming that $\partial\theta/\partial p$ is constant (and equal to $\partial\theta/\partial p|_{z=0}$) throughout the troposphere and inverting (2) with γ_c replacing γ_m. This moist critical lapse rate is then compared with the critical lapse rate predicted by baroclinic instability theory. The critical lapse rate used for convective adjustment is the smaller of the two. Once the critical lapse rate is determined, the convective adjustment scheme described by Wang et al. (1984) is used to ensure that all levels are statically stable with respect to the critical lapse rate.

The rationale for assuming $\partial\theta/\partial p$ is constant throughout the troposphere is based on two primary factors. First, the scheme described above gives a better simulation of the tropical temperature profile than the moist adiabatic lapse rate used by Stone and Carlson (1979). Second, as noted by Rennick (1977), an empirical fit of the observed lapse rates match a constant $\partial\theta/\partial p$ profile much better than the assumed constant $\partial T/\partial z$ profile, which is often used.

TABLE 1. Greenhouse gas concentrations used for the steady state simulations I, II, and III. These concentrations are identical to those used in M94.

	Simulation		
	I	II	III
CO_2 (ppmv)	334	350	350
CH_4 (ppbv)	1538	1685	1685
N_2O (ppbv)	300	308	308
CFC-11 (pptv)	149	253	253
CFC-12 (pptv)	250	434	434
O_3	1979	1979	1990

3. Climate sensitivity to a doubling of CO_2

a. The control run (1979)

For the control run climate simulation we use the same realistic 1979 greenhouse gas concentrations as in M94; see simulation I in Table 1. To ensure a steady-state climate, we perform a 20-yr simulation run and use the mean of the last 5 yr of this simulation as the control climate year. For example, day 1 (1 January) of the control climate year is the arithmetic mean of day 1 from the last 5 yr of the simulation.

The optical depths of low and middle clouds, and the thermal diffusion of the mixed layer ocean are used to tune the model's surface temperature and seasonal sea-ice area coverage to the observed climate. The global-mean annual-average surface air temperature and planetary albedo simulated by the model are 287.380 K and 0.296, respectively; both in good agreement with observations. For the simulations reported throughout this paper the precision in global mean annual average surface air temperature is conservatively estimated to be 0.002 K. Figure 2 shows the simulated zonal mean surface air temperatures for annual, winter (DJF), and summer (JJA) averages compared to the observations reported by Willmont and Legates (1993). Inspection of Fig. 2 shows good agreement between the simulated

Unauthenticated | Downloaded 10/21/21 05:38 AM UTC

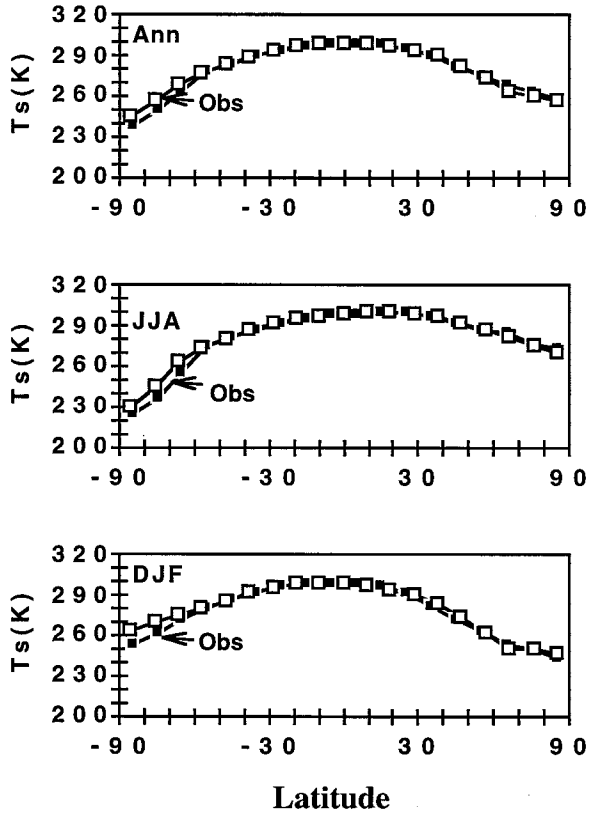

FIG. 2. Zonal-mean, annual summer (JJA) and winter (DJF) surface air temperature. Observations are from Willmott and Legates (1993).

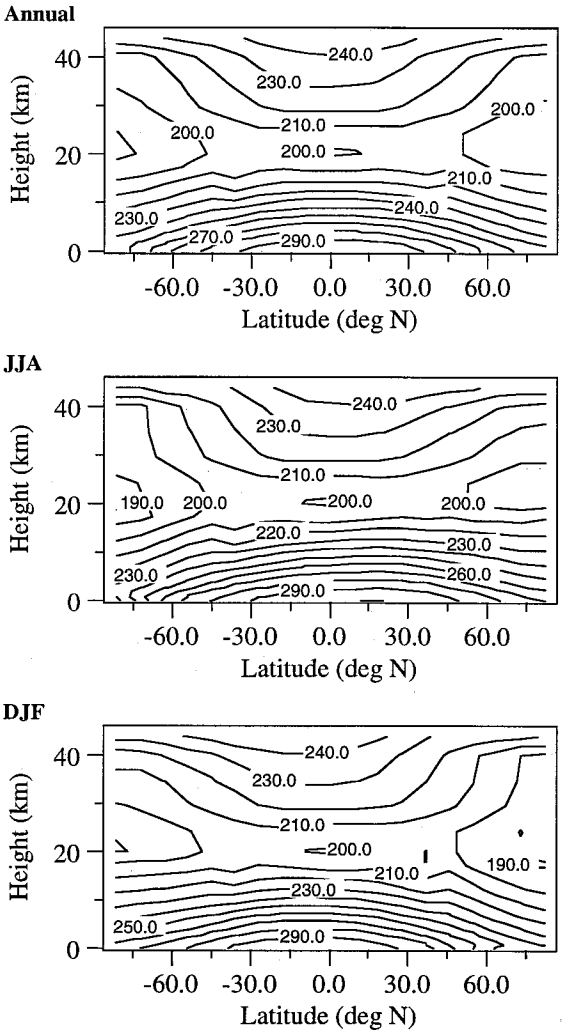

FIG. 3a. Zonal-mean temperature profile simulated by the 19-zone ASRD for annual, JJA, and DJF means. Contour intervals are 10 K and heights are approximate.

and observed surface air temperature for all seasons. The simulated two-dimensional temperature fields are shown in Fig. 3a for annual, JJA, and DJF averages and the corresponding observations are shown in Fig. 3b. The model simulates the seasonal cycle and magnitude of tropospheric temperatures well. However, the simulated temperatures in the stratosphere near 25 km are too low, especially in the summer hemisphere.

Figure 4 shows the control run simulation of sea ice area coverage compared with NMC observations for the period 1978–88. The amplitudes and annual mean values of the simulated sea ice fluctuations in each hemisphere agree well with the observations. However, there are some features of the observed sea ice cycle, such as shape and timing of the maximum and minimum sea ice cover, that the model does not simulate very well at present. Future versions of the ASRD-19 model will include a more advanced treatment of sea ice physics to capture additional features of the observed sea ice cycle and, hence, better simulate the feedbacks between changes in sea ice and surface temperature.

b. 2 × CO_2 experiment

To further examine the model's performance we have performed a steady-state CO_2-doubling experiment. Since this is a standard experiment performed with climate models, we use it as a bench mark of the sensitivity of our 2D climate model. We compare the mean of the last 5 yr of the 20-yr control run described above, [CO_2] = 334 ppmv, to that of a run with a fixed CO_2 concentration of 668 ppmv (2 × CO_2). There are several feedback processes included in this experiment. These include changes in atmospheric water vapor (fixed relative humidity), meridional heat transport in both the atmosphere and oceans, atmospheric lapse rate, sea ice cover (ocean sector albedo), and land surface albedo. A potentially important feedback, which has not been included in this work, is that associated with change in cloud cover, cloud height, or cloud microphysical properties. Cess et al. (1996) have assessed the treatment of cloud feedback in general circulation models (GCMs) and show that most GCMs presently simulate ''modest'' cloud feedback strength and that they do so for different

Unauthenticated | Downloaded 10/21/21 05:38 AM UTC

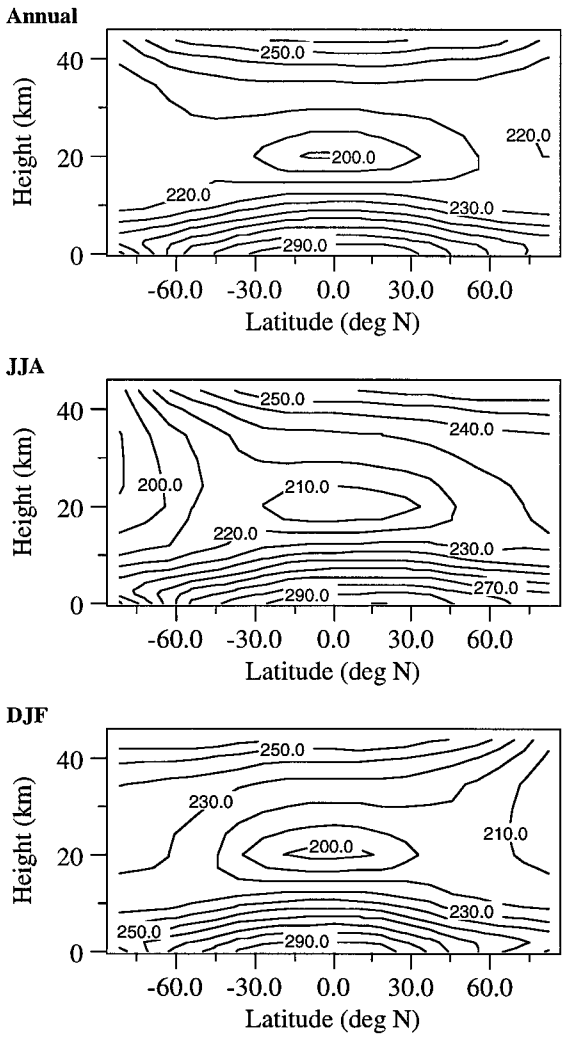

FIG. 3b. Zonal-mean observed temperature profile for annual, JJA, and DJF means. Contour intervals are 10 K. Observations from NCAR Data Support Section, Scientific Computing Division.

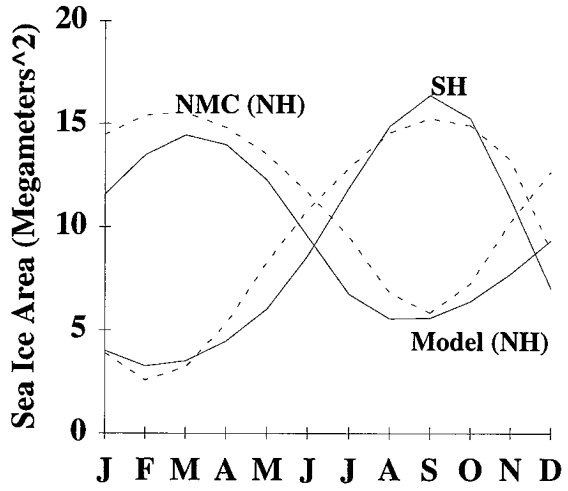

FIG. 4. The annual cycle of model-simulated sea-ice area coverage for the Northern and Southern Hemispheres (units are 10^6 km^2). NMC observations are dashed lines and simulated values are solid.

physical reasons. Until we incorporate techniques into the ASRD-19 for predicting relevant cloud properties based on model state variables (temperature, pressure, relative humidity, aerosol loading) and test the validity of these techniques in the 2D model structure, using prescribed cloud properties is the best alternative.

The $2 \times CO_2 - 1 \times CO_2$ changes in surface air temperature simulated by our model are shown in Fig. 5. The change in global-mean annual-averaged surface air temperature, ΔT_s, simulated by the model is 2.6 K. This compares well with the range of 1.5–4.5 K given by the IPCC 1990 with a ''best guess'' of 2.5 K. Reflected in this 2.6 K increase in global-mean surface air temperature is a 2% decrease in annual-averaged global-mean albedo. This 2% decrease in planetary albedo is equivalent to an approximate 1% (2.13 W m^{-2}) increase in absorbed solar energy, or a forcing about half as large as that due to doubling CO_2. The global-mean albedo change is greatest during late spring and early summer of each hemisphere May–July, and November–January, reflecting an earlier breakup each year of surface ice and snow cover in the $2 \times CO_2$ run compared to the $1 \times CO_2$ run. The simulated $2 \times CO_2 - 1 \times CO_2$ temperature change of 2.6 K simulated by the ASRD-19 is about 54% higher than that simulated by the three-zone model of M94 (1.7 K). Inclusion of the sensitive high latitudes and an interactive sea ice model both contribute to the greater climate sensitivity of the ASRD-19 relative to the three-zone model of M94.

Figure 5 also shows that the annually averaged simulated $2 \times CO_2 - 1 \times CO_2$ surface air temperature increase at the poles is two to three times greater than in the Tropics and that this amplified warming in the polar region is greatest during winter in the Northern Hemisphere. In an analysis of the response of their 18-zone 2D statistical dynamical climate model, MacKay and Khalil (1995) analyzed the diagnostic output of their model and identified several mechanisms responsible for the larger ΔT_{CO_2} at the poles relative to

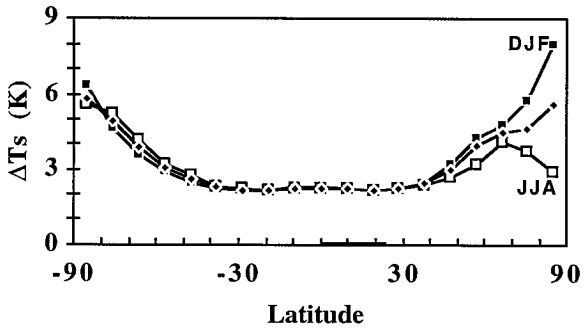

FIG. 5. The $2 \times CO_2 - 1 \times CO_2$ surface air temperature change, ΔT_s, simulated by the ASRD-19 model for winter (DJF), summer (JJA), and annual means.

Unauthenticated | Downloaded 10/21/21 05:38 AM UTC

the Tropics. Among these were: regions with low surface temperatures are naturally more sensitive to a given forcing than warm regions ($\Delta T_g \ \alpha \ T_g^{-3}$);[2] reduction in solar energy reaching the surface in the Tropics for 2 $\times$ CO_2, differences in static stability between the Tropics and polar region, lapse rate feedback, and dynamical heat transport, which helps maintain the temperature structure of the atmosphere. These processes also contribute to the response of our 2D energy balance model. However, for our model ΔT_s is larger than the model of MacKay and Khalil by at least 70% at all latitudes. The greater climate sensitivity of our model is primarily due to the much larger polar warming (primarily associated with sea ice changes), which is in turn propagated to other latitudes by meridional heat transport changes.

The simulated latitudinal and seasonal structure of the 2 $\times$ CO_2 $-$ 1 $\times$ CO_2 temperature change (Fig. 6) has several characteristics in common with general circulation model simulations (e.g., see Held 1993) and other two-dimensional climate models (e.g., MacKay and Khalil 1995). In particular, the ASRD-19 has amplified warming at the poles, a small local warming maximum in the upper troposphere of the Tropics and substantial stratospheric cooling.

One feature present in both our 2D model and the 2D model of MacKay and Khalil (1995) is that the difference between high-latitude winter surface warming and summer surface warming is much more pronounced for the Northern Hemisphere than for the Southern Hemisphere. Many GCM simulations also exhibit this interhemispheric asymmetry (see Washington and Meehl 1993 or Colman et al. 1994). There is little difference between the two hemispheres for the change in annual mean surface air temperature. As noted by MacKay and Khalil (1995) this seasonal interhemispheric asymmetry is fundamentally related to the greater land fraction (lower thermal inertia) of the Northern Hemisphere relative to the Southern Hemisphere. The interhemispheric asymmetry of thermal inertia and surface albedo results in differences in the static stability and in the overall temperature structure of the two hemispheres and, hence, their different seasonal responses. To confirm that this is also the case in our model (as opposed to differences in cloud cover or relative humidity), we performed an experiment in which we used symmetric land fractions at each latitude zone based on the Northern Hemisphere land fractions, keeping all other prescribed values the same as in the control run. This eliminated the interhemispheric asymmetry, resulting in Southern and Northern Hemisphere responses quite similar to that shown in Fig. 6 for the Northern Hemisphere.

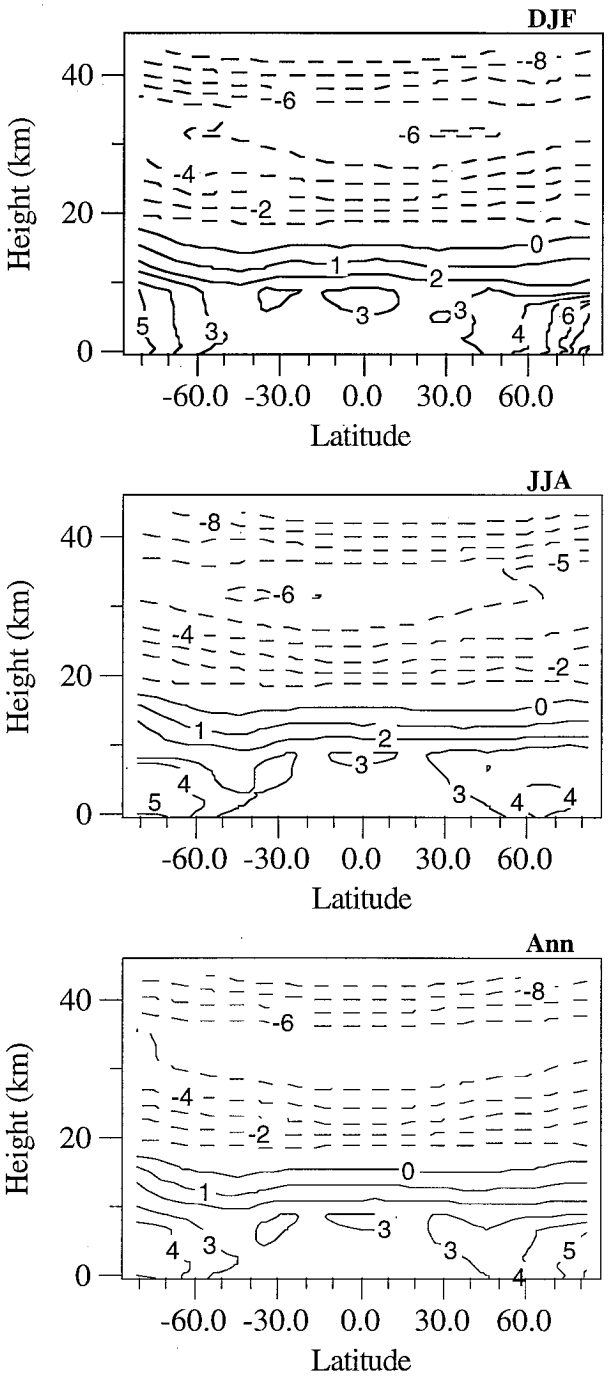

FIG. 6. The calculated two-dimensional temperature (2 $\times$ CO_2 $-$ 1 $\times$ CO_2) changes for annual, DJF, and JJA means. Units are Kelvin and temperature changes less than zero are shown by dashed lines.

4. Climatic effect of ozone

One of the primary objectives of this paper is to estimate the steady-state climatic effect of sustained ozone changes, similar to those observed from 1979 to 1990, relative to the sustained changes in the other greenhouse gases over the same time period. To accomplish this

[2] The subscript *g* stands for the ground, which is assumed to be a blackbody for infrared radiation.

Unauthenticated | Downloaded 10/21/21 05:38 AM UTC

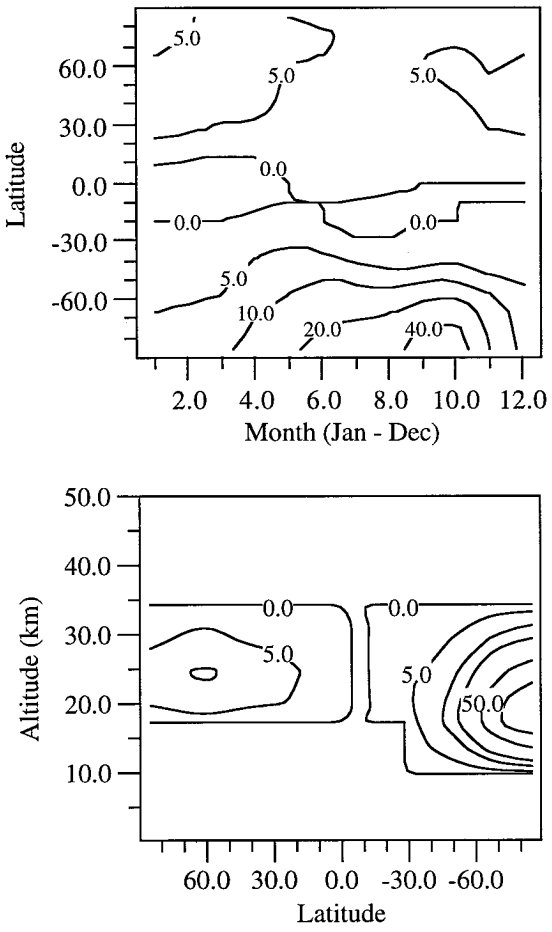

FIG. 7. The assumed 1979–90 percent reduction in column ozone as a function of latitude and season (top) and the October latitude height profile of percent reduction in ozone used for the simulations reported (bottom).

task, we perform three steady-state simulations to calculate the 1979–90 changes in radiative forcing and steady-state surface air temperature with and without lower stratospheric ozone losses: (I) 1979 greenhouse gas concentrations and 1979 ozone, (II) 1990 greenhouse gas concentration with 1979 ozone, and (III) 1990 greenhouse gas concentrations with 1990 ozone (see Table 1). We again use the average over the last 5 yr of the 20-yr simulation of the seasonal means to represent the steady-state climate.

In the fixed ozone experiment (FOE), we calculate the change in atmospheric temperature and adjusted forcing simulated by the model for the changes in greenhouse gases observed between 1979 and 1990 using a 1979 (seasonally variable) baseline ozone profile obtained from solar backscattered ultraviolet (SBUV) measurements (FOE is the difference between simulations II and I above). Our second experiment, which we call the variable ozone experiment (VOE), is identical to experiment A performed in M94. The VOE is the same as the FOE except that we use the 1979 baseline ozone

TABLE 2. The global-mean annual-average change in surface air temperature ($\langle \Delta T_s \rangle$), adjusted forcing ($\langle \mathrm{AF} \rangle$), and sensitivity factor ($\mathrm{SF} = \langle \Delta T_s \rangle / \langle \mathrm{AF} \rangle$) for the 19-zone and 3-zone models for the experiments described in the text. $2CO_2$, FOE, VOE, and ΔO_3 are as defined in the text.

	19 z			3 z		
Exp	ΔT_s (K)	AF (W m^{-2})	SF (K W^{-1} m^2)	ΔT_s (K)	AF (W m^{-2})	SF (K W^{-1} m^2)
$2CO_2$	2.627	4.11	0.64	1.7	*	*
FOE	0.272	0.418	0.65	0.20	0.443	0.45
VOE	0.165	0.359	0.46	0.15	0.367	0.41
ΔO_3	−0.107	−0.059	1.81	−0.05	−0.076	0.66

* Not reported in M94.

profiles altered by the estimated 1979–90 percent changes in lower-stratospheric ozone (VOE is the difference between III and I above). The annual average 2D temperature profile of the steady-state climate for 1979 trace gas concentrations is that shown in Fig. 3a.

The distributions of 1979–90 ozone change used in M94 were inferred from TOMS data. Since the development of the ASRD-19 model was underway at the time of the three-zone model experiments of M94, the seasonal and vertical distributions of percent ozone change used in M94 were first estimated for a grid that is identical to the present 19-zone model grid; averages were then taken to obtain the ozone distributions used for the three-zone experiments. Thus the percent ozone changes used here for the VOE are identical to those used in M94 for their experiment A. This makes the comparison between the two models more meaningful. The top panel of Fig. 7 shows the assumed changes in column ozone as a function of latitude and season used and the bottom panel gives the latitude height profile of ozone change for the most extreme month, October.

We begin by comparing the response of the ASRD-19 to that of the M94 three-zone model for each experiment described above. Table 2 gives the global average annual mean values of surface air temperature change and net adjusted radiative forcing for the different experiments performed with the 19-zone and 3-zone models. We follow the standard convention for the calculation of net adjusted radiative forcing (Molnar et al. 1994; IPCC 1994; or Ramaswamy et al. 1992). The change in net adjusted radiative forcing at the tropopause due to a perturbation in atmospheric composition is calculated as follows. After a specific perturbation in atmospheric composition, the model is run for six years with fixed tropospheric temperatures (and albedo) while allowing stratospheric temperatures to radiatively readjust (fixed dynamical heating) to their new steady-state values. The change in net (solar + terrestrial) radiation at the tropopause is then calculated as the difference between the net radiation into the troposphere (downward taken as positive) for the steady-state conditions before the perturbation and the steady-state conditions at the end of

Unauthenticated | Downloaded 10/21/21 05:38 AM UTC

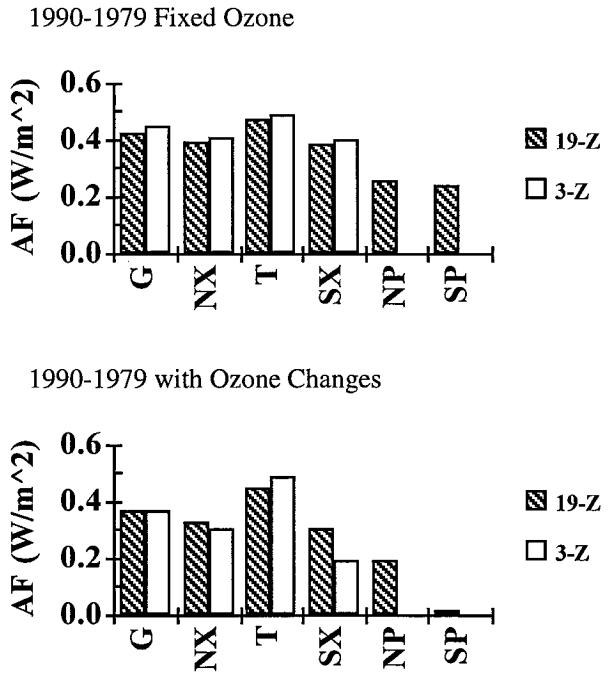

FIG. 8. The annual mean adjusted forcing for the 19-zone and 3-zone models averaged over different zones. G: Global average, NX: Northern extratropics, T: Tropics, SX: Southern extratropics for the 3- and 19-zone models. Also the north and southern polar regions, NP and SP, corresponding to 60°–90° are given for the 19-zone model. Units are watts per square meter.

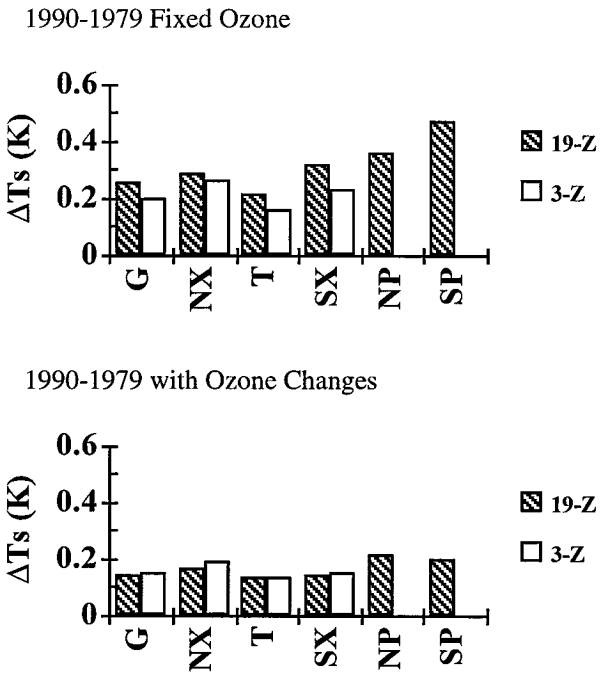

FIG. 9. As in Fig. 8 but for the change in surface air temperature ΔT (units are K).

the 6-yr run. As in M94 we use 100 and 200 mb for the tropical (33°S–33°N) and extratropical tropopause, respectively.

Figure 8 shows the annual mean adjusted forcing simulated by the 3-zone and 19-zone ASRD models for 1990 − 1979 greenhouse concentration changes of the FOE (top) and VOE (bottom) at the specified latitude zones. In addition to the global (G), northern extratropical (NX), tropical (T), and southern extratropical (SX) averages for both the 3- and 19-zone models, we have also included the averages of the north and south polar regions (NP and SP) of the 19-zone model. Since the assumed ozone changes are largest near the South Pole, including this additional information is useful in understanding the behavior of the 19-zone model. For the FOE, the adjusted forcing simulated by the two models are in close agreement with each other for all zones. The global average forcing is 0.418 W m^{-2} and 0.443 W m^{-2} for the 19- and 3-zone models, respectively. For both models the fixed ozone adjusted forcing is greatest in the Tropics, reflecting the higher atmospheric temperatures there. The 19- and 3-zone adjusted forcing for the VOE are 0.359 W m^{-2} and 0.367 W m^{-2}, respectively; see Table 2. The difference between the adjusted forcing for the VOE and FOE (or simulations III−II) is the adjusted forcing from the ozone perturbation only: −0.059 W m^{-2} and −0.076 W m^{-2} for the 19- and 3-zone model, respectively. The intermodel (19- vs 3-zone) difference is largest for the ozone only forcing. This is primarily because of the strong latitudinal dependency of the assumed ozone changes combined with the large difference in latitudinal resolution of the two models. For example, the near zero net adjusted forcing simulated by the 19-zone model for the southern polar region (SP = 62°–90°S) cannot be simulated (or inferred) by the 3-zone model because the magnitude of the decrease in ozone concentration averaged over the southern extratropics (SX = 24°–90°S) is too small. That is, since the distribution of ozone change has significant structure on scales smaller than the 3-zone model resolution, some aspects of the climatic effects of ozone change are missed by the 3-zone model.

The zonally averaged mean steady-state surface air temperatures, ΔT_S, for the two experiments are shown in Fig. 9, FOE (top) and VOE (bottom). The global-mean annual-averaged change in surface temperature for the 19-zone model is 0.272 K and 0.165 K for FOE and VOE, respectively; Table 2. Thus, the assumed reductions in lower-stratospheric ozone result in an absolute decrease in global mean annual average surface warming of 0.107 K.

As mentioned previously, the sensitivity of the two models to a doubling of atmospheric CO_2 are different, 2.6 K for the 19-zone model and 1.7 K for the 3-zone model. This is reflected in the difference between the two models' simulated fixed ozone experiment temperature changes. Similar to the response of the double CO_2 experiment, the greenhouse warming simulated by the 19-zone model is greater at high latitudes than in the

Unauthenticated | Downloaded 10/21/21 05:38 AM UTC

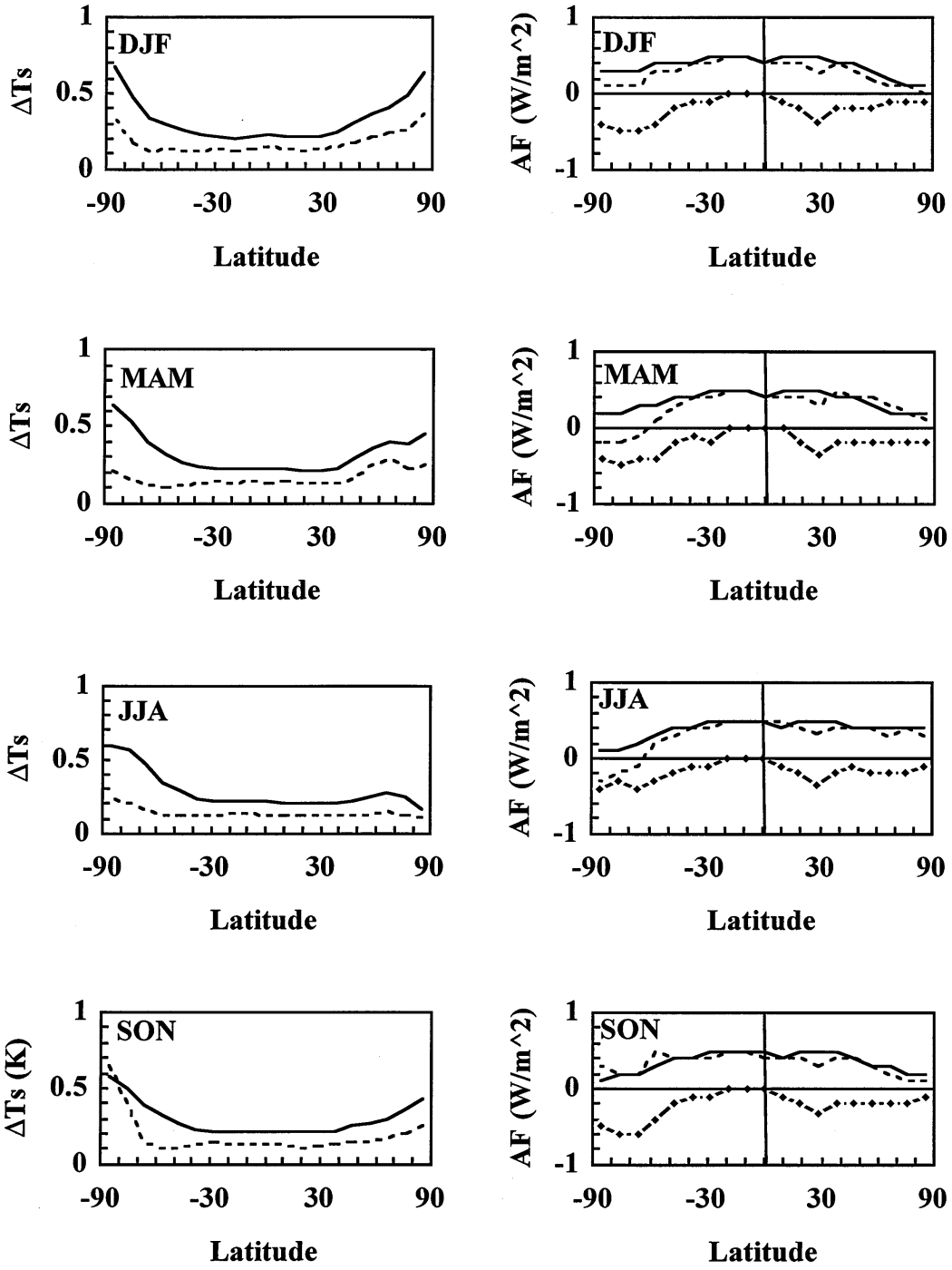

FIG. 10. Left: steady-state surface air temperature change (K) for 1990 − 1979 greenhouse gas changes: FOE is solid and VOE is dashed. Right: Adjusted forcing(W m^{-2}); 1990 − 1979 fixed ozone (FOE) (solid), 1990 − 1979 (VOE) (dashed), VOE-FOE (ozone forcing) for infrared radiation only (solid diamonds).

Tropics for the FOE; see Fig. 9. Since the assumed lower-stratospheric ozone reductions are greatest at high latitudes, the difference between the adjusted forcing of the FOE and the VOE are typically greatest at high latitudes. Hence the simulated temperature changes at high latitudes are typically altered the most by the ozone changes. However, as discussed below, this statement is not without caveats.

The simulated steady-state changes in surface air temperature and adjusted forcing for the two experiments are presented in Fig. 10 for DJF, MAM, JJA, and SON seasonal means. It is clear from an analysis of Fig. 10

Unauthenticated | Downloaded 10/21/21 05:38 AM UTC

TABLE 3. Percent composition $(1 - \Delta X_A/\Delta X_{\text{fixed O3}}) \times 100\%$ for the 19-zone and 3-zone models, where X is either adjusted forcing AF or surface air temperature T_s: G (90°N–90°S), NX (90°–24°N), T (24°N–24°S), SX (24°S–90°S), NP (90°–62°N), SP (62°–90°S). [For the 3-zone model NX (90°–30°N), T (30°N–30°S), SX (30°S–90°S)].

Experiment	G	NX	T	SX	NP	SP
AF						
19-zone	−14	−16	−5	−23	−25	−94
3-zone	−17	−24	0.4	−52		
T_s						
19-zone	−39	−38	−34	−50	−39	−54
3-zone	−28	−27	−22	−36		

that the relation between adjusted forcing and surface temperature change is highly nonlinear. For example, even though the adjusted forcing is very small at the equator when ozone changes are included in the simulation, the surface temperature near the equator decreases significantly. As noted by M94, the reduced temperatures at higher latitudes tend to enhance the meridional heat transport out of the Tropics, which in turn results in an indirect cooling of the Tropics. The global mean annual average sensitivity factors ($\langle \Delta T_S \rangle / \langle AF \rangle$) for each model and each experiment are also given in Table 2. The ozone only sensitivity is calculated from the difference in temperature changes and adjusted forcing between simulations III and II of Table 1 (or VOE–FOE). It is worth noting that the sensitivity factor for the FOE is 0.65 K W^{-1} m^2, which is close to the 2 × CO_2 sensitivity of 0.64 K W^{-1} m^2 (2.63 K/4.11 W m^{-2}). This agreement is expected since there is no latitudinal variation of the trace gas perturbation in either of these simulations. As for the 2 × CO_2 results, the difference between the sensitivity of the ASRD-19 and the 3-zone ASRD for the FOE is a result of the prognostic determination of sea ice in the ASRD-19 and the inclusion of the sensitive high latitudes, which tend to amplify the global sensitivity. For both models the ozone-only sensitivity is largest. Below we discuss the intermodel differences and intramodel differences in more detail.

Similar to M94, we define the percent ozone compensation of adjusted forcing (AF) due to ozone changes as $[(AF_{O_3\ \text{fixed}} - AF_{\text{with}\ O_3\ \text{changes}})/AF_{O_3\ \text{fixed}}] \times 100\%$ and the percent compensation for temperature change analogously. The percent compensations of each model to the annual-mean adjusted forcing and temperature are shown in Table 3. For each model the percent compensation in temperature has little spatial variation in the Northern Hemisphere and Tropics. The largest percent compensation occurs in the southern extratropics where the assumed ozone losses are greatest. Although some spatial variability does exist in the surface air temperature response to a given forcing, changes in meridional heating significantly reduces the spatial variability of surface air temperature relative to that of the adjusted forcing. Our results indicate that the percent compensation to the global averaged annual mean surface air temperature warming due to ozone depletion is 39% (0.107 K/0.272 K). This is about 1.4 times larger than the 28% compensation reported in M94. Table 2 clearly shows the point stressed by M94; the adjusted forcing is a poor proxy for the response of the climate system.

Although its potential importance was stressed in M94, an investigation of the seasonal influence of ozone changes was not included in that study. Ozone losses in the lower stratosphere typically correspond to a decrease in adjusted forcing of the surface–troposphere system (Lacis et al. 1990). However, during the spring of each hemisphere the assumed ozone reduction can actually result in an increase in the adjusted forcing for the extratropics. For global-mean conditions, the decrease in longwave adjusted forcing at the tropopause is indeed greater in magnitude than the increase in shortwave forcing accompanying ozone reductions below approximately 30 km, but the situation is more complex when the seasonal cycles of atmospheric temperatures and incident solar intensity are considered. The change in the flux of longwave radiation at the tropopause is highly dependent on the effective radiating temperature of the atmosphere. In the spring, when atmospheric temperatures are still relatively cold, the change in longwave forcing for a given ozone change will be smaller than when the atmospheric temperatures are warmer, as in the summer. Although the positive solar forcing for a given ozone decrease in the lower stratosphere is typically smaller in magnitude than the corresponding negative longwave adjusted forcing, in the spring at high latitudes before the atmospheric temperatures increase, the positive solar forcing does indeed outweigh the longwave forcing. At most latitudes, as tropospheric temperatures are also allowed to adjust, a decrease in ozone does however result in a net cooling of the surface. However, for the southernmost zone (80°–90°S), the small amount of low and middle cloud prescribed for this zone enhances the increase in solar energy reaching the surface due to ozone loss. The high static stability of this zone is also conducive to large surface air temperature increases. Thus, the timing of the maximum in the ozone hole, the small amount of low and middle level clouds prescribed for the southernmost zone, and its high static stability results in an increase in the 80°–90°S surface air temperature for the VOE relative to the FOE (see Fig. 10) during SON.

These results illustrate the potentially large influence of the temporal and spatial distribution of perturbations in atmospheric composition to the climate sensitivity. For example, Daniel et al. (1995) estimated the global warming potentials of halocarbons by considering the warming from them and the indirect cooling from the assumed ozone loss resulting from halocarbon increase. Our results suggest that simply using global-mean net adjusted radiative forcing as an estimate of the climatic effects due to halocarbon-induced ozone perturbations is not accurate.

It is important to understand how a relatively small

Unauthenticated | Downloaded 10/21/21 05:38 AM UTC

change in global-mean adjusted forcing (-0.059 W m^{-2}) can result in such a large compensation in global-mean steady-state surface temperature increase (-0.107 K), that is, a sensitivity factor of 1.81 K W^{-1} m^2 compared to 0.64 K W^{-1} m^2 for $2CO_2$. There are several possible explanations that we have explored: One possible explanation is that radiative forcings localized at higher latitudes tend to make the global climate sensitivity greater simply because high latitudes are more sensitive than lower latitudes. We performed an experiment to test this as a possible mechanism. Using simulation I as the initial control run, we doubled the CO_2 concentration between 60° and 90°S only and ran to steady state. For this simulation we calculated the global-mean sensitivity factor to be 0.83 K W^{-1} m^2) ($\Delta T_S = 0.155$ K and AF $= +0.186$ W m^{-2}). Thus, this high-latitude forcing did result in an increase of about 30% in the global-mean sensitivity factor above the uniform double CO_2 case. A perturbation in stratospheric aerosols confined to 60° to 90°S gave similar results. Since the sensitivity factors for these perturbations are still much smaller than the sensitivity factor for the assumed ozone perturbation, this simple explanation does not completely explain the large sensitivity to our assumed ozone perturbations.

Molnar and Gutowski (1995) and Wang et al. (1984) have emphasized the connection between meridional heat transport and climate sensitivity. Our analysis suggests that this is particularly important in regards to ozone loss in the lower stratosphere at high latitudes. We have performed several other experiments in an attempt to better understand the role that meridional heat transport feedback has on the climate sensitivity. The notation of Lacis and Mishchenko (1995) is used to quantitatively estimate the feedback efficiency factor of the meridional heat transport (MHT) feedback (f_{MHT}):

$$\Delta T_a = \Delta T_o + f_{\mathrm{MHT}} \Delta T_a, \tag{3}$$

where ΔT_a is the equilibrium temperature change when all model feedbacks are included, and ΔT_o is the equilibrium temperature change for the base case, all feedbacks except MHT feedback. Solving (3) for the feedback efficiency factor gives

$$f_{\mathrm{MHT}} = \left[1 - \frac{\Delta T_o}{\Delta T_a}\right]. \tag{4}$$

If $\Delta T_a < \Delta T_o$, the feedback efficiency factor is negative as is the case with the decrease in O_3 at high latitudes when the poleward flow of meridional heat transport increases in response to high-latitude cooling. This increased heat transport directly limits the high-latitude cooling through increased convergence of energy into the high latitude regions and indirectly limits high-latitude (and global) cooling by weakening the strength of the temperature–albedo feedback. Table 4 shows the results of the 1979–90 (simulations II to III, ΔO_3) steady-state conditions with and without MHT feedback: $f_{\mathrm{MHT}} = -4.65$. This and the $0.8CO_2$ experiment shown in Table 4 ran for 6 yr with simulation II conditions, the step perturbation (with or without MHT feedback) is imposed at the end of year 6, and the run continued for 24 more years to a new steady state.

TABLE 4. Meridional heat transport feedback. Perturbations used 1990 with 1979 ozone as the initial atmospheric state. $0.8CO_2$ 60°S–90°S: CO_2 reduction from 350 to 280 ppmv confined to latitudes between 60° and 90°S; ΔO_3: 1990–79 ozone perturbation ΔT are global-mean annual average surface air temperature changes (precision is conservatively estimated at 0.002K).

Perturbation	$0.8CO_2$ 60°S–90°S	ΔO_3
ΔT_a (All feedbacks)	-0.042	-0.107
ΔT_o (Fixed MHT)	-0.454	-0.605
f_{MHT}	-9.81	-4.65
ΔSW (W m^{-2})	0.042	0.088*

* The net increase in SW radiation leaving the top of the atmosphere is 0.246 W m^{-2} of which 0.158 W m^{-2} is from the initial ozone change with no change in tropospheric temperature.

To see whether there is anything special about the forcing from O_3, we perform a CO_2 reduction experiment with the perturbation confined to high latitudes, with and without MHT feedback included. In the $0.8CO_2$ perturbation the concentration of CO_2 is reduced by 20% of its FOE value (from 350 to 280 ppmv) and the perturbation is confined between 60° and 90°S (all other latitudes had no change in atmospheric composition). The adjusted forcing at the tropopause for this perturbation is -0.058 W m^{-2}, which is comparable to the difference in adjusted forcing between simulations III and II (O_3 only forcing) discussed above, -0.059 W m^{-2}. For this experiment the MHT feedback greatly limits the high latitude (and global) cooling: $f_{\mathrm{MHT}} = -9.81$. Interestingly, f_{MHT} of the $0.8CO_2$ perturbation confined to high southern latitudes is twice that of our assumed ozone perturbations, which are also largest at high southern latitudes.

Also shown in Table 4 are the changes in reflected solar radiation at the top of the atmosphere (ΔSW) for each run with MHT included. Since ΔSW is directly related to the change in planetary albedo, this provides an estimate of the net temperature albedo feedback. Of the 0.246 W m^{-2} increase in reflected solar radiation (energy loss from system) 0.158 W m^{-2} is due to the ozone changes alone (without changes in surface temperature, surface albedo, or atmospheric water vapor), the rest (0.088 W m^{-2}) is related to temperature albedo feedback. Essentially all of the 0.042 W m^{-2} increase in reflected solar radiation is from the temperature albedo feedback for the $0.8CO_2$ perturbation. The net effect of the temperature albedo feedback is about 2.3 times larger for the ozone perturbation than for the $0.8CO_2$ perturbation confined to high latitudes. This larger temperature albedo feedback is consistent with the weaker negative MHT feedback discussed above.

Understanding why the magnitude of the negative MHT feedback is weaker for our assumed ozone per-

Unauthenticated | Downloaded 10/21/21 05:38 AM UTC

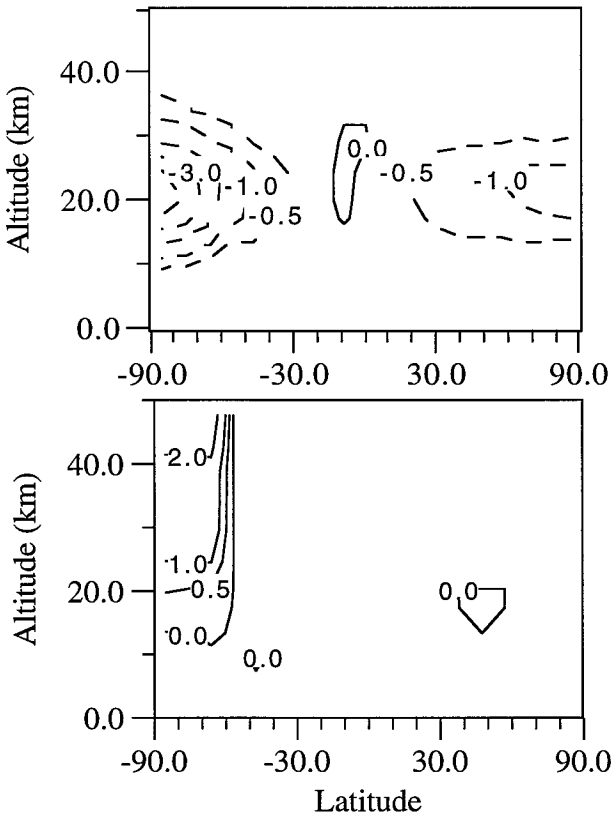

FIG. 11. The 2D change in annual-mean temperature due to ozone perturbation VOE (1990 greenhouse gases with 1990 ozone) − FOE (1990 greenhouse gases 1979 ozone), top, and for .8CO2 confined between 60° and 90°S, bottom.

turbations is an interesting question. A plausible qualitative argument, which is consistent with the results of the simulation experiments performed, is outlined here. Changes in both the meridional heat transport and the infrared opacity of the lower stratosphere accompanying the assumed high-latitude ozone loss tend to enhance the global climate sensitivity factor as follows: The initial response to the radiative forcing is a large cooling at high latitudes; Fig. 11 (top panel). This results in an increase in the equator to pole temperature gradient causing an increase in the meridional heat transport from the Tropics to high latitudes. For the assumed ozone perturbation the tropospheric temperature gradient increase is greatest near the tropopause (i.e., in the vicinity of the largest ozone losses). Thus, the increase in meridional heat transport is relatively large in the upper troposphere. The MHT stabilizes when high latitude temperatures readjust to the net heating/cooling. The decreased infrared opacity of the lower stratosphere (associated with ozone loss at the same location) increases the ability of the upper troposphere to radiatively cool into space. As a result, more energy is transported from the Tropics, leading to a larger global cooling.

Figure 11 shows the steady-state temperature change associated with ozone loss, ΔO_3 (top), and $0.8C0_2$ (bottom) for comparison. In contrast to the ozone perturbation, the increased lower-stratospheric temperatures from CO_2 loss reduces the upper-tropospheric meridional temperature gradients forcing more of the energy flow out of the Tropics to be closer to the surface. This more effectively controls the increase in surface albedo associated with decreasing high latitude temperatures.

5. Conclusions

The physics and performance of the most recent version of the AER two-dimensional seasonal radiative dynamical climate model has been described. We show that the model simulates many features of the present climate system rather well. The model's sensitivity to a doubling of atmospheric carbon dioxide in regards to the global mean annual average change in surface air temperature is 2.6 K. We also find that the $2 \times CO_2 - 1 \times CO_2$ temperature change simulated by our model has many of the spatial and temporal features found in other climate models.

We have estimated the climatic effects of sustained ozone changes relative to the other greenhouse gases and have found that including decreases in stratospheric ozone (similar to those observed from 1979 to 1990) in the steady-state climate simulation reduces the modeled greenhouse warming by 39% relative to the fixed ozone case. We attribute much of this large compensation in global-mean annual-averaged greenhouse warming, resulting from the relatively small global-mean annual-averaged adjusted forcing, to increases in high-latitude meridional heat transport in the upper troposphere coupled with the low infrared opacity of the lower stratosphere, both a result of ozone loss in the lower stratosphere at high latitudes. There are significant differences between the simulations reported here and those reported by M94, who used a similar model but of much lower latitudinal resolution. Because both ozone changes and the model's climate sensitivity are greatest at high latitudes, using a model of appropriately high latitudinal resolution is essential when simulating the latitudinal and seasonal effects of recent ozone changes. The primary difference between the global-mean annual-averaged surface temperature compensation between our simulation and that of M94 (39% compared to 28%) is also attributable to an inability of the low-resolution model to simulate the influence of the locally large ozone losses at high latitude.

Our steady-state results suggest that the lower-stratospheric ozone decreases observed between 1979 and 1990 may have partially offset the greenhouse warming due to increases in the other greenhouse gases over the past century. It is worth noting here that we also performed a steady-state simulation in which only CFC-11 and CFC-12 were allowed to change from their 1979 to 1990 values; other gases, including ozone, were held at their 1979 concentrations. This simulation resulted in a global-mean annual-averaged surface temperature

Unauthenticated | Downloaded 10/21/21 05:38 AM UTC

change of 0.04 K. Thus, if we assume that the ozone losses are a direct result of these CFCs supplying chlorine to the stratosphere, we obtain a net steady-state cooling of the climate from CFC loading in the atmosphere. Assuming that the partitioning of the greenhouse warming from different greenhouse gases for the net steady-state greenhouse warming is qualitatively similar to the partitioning for the transient greenhouse warming, our simulations suggest that the compensation to greenhouse warming due to ozone loss may be greater than the warming associated with the CFC increases. Consequently, it is plausible that ozone losses have partially masked the greenhouse warming over the last 10–15 yr. Thus, the phaseout of CFCs and the associated rebound in ozone levels over the next several decades could result in an accelerated global warming for this time period beyond what would be expected from changes in the other greenhouse gases alone.

Although our model results are very robust to small changes in model physics, the uncertainties in the spatial and temporal distribution of the ozone losses, especially near the tropopause, and uncertainties in the present ability of any model to simulate the real world make our results correspondingly uncertain. However, we are confident that our results indicating the importance of large losses of high-latitude lower-stratospheric ozone to the global climate signal are qualitatively valid. It is also apparent from our results that the influence of the latitude, height, and seasonal timing of a particular radiative perturbation (greenhouse gas or aerosols) is very complex and hence deserves further investigation.

Acknowledgments. The authors thank N.-D. Sze, R. Rosen, D. Weisenstein, C. Scott, and M. Danilin of AER, Inc. for their insightful discussions and comments. The suggestions of J. A. Coakley Jr. and two anonymous referees also greatly improved the final manuscript. This work was supported by grants from the Carbon Dioxide Research Program, Office of Health and Environmental Research, U.S. Department of Energy (DE-FG02-86ER60485), and NASA Atmospheric Chemistry Modeling and Data Analysis Program (NASW-4775).

REFERENCES

Breigleb, B. P., P. Minnis, V. Ramanathan, and E. Harrison, 1986: Comparison of regional clear-sky albedos inferred from satellite observations and model computations. *J. Climate Appl. Meteor.*, **25,** 214–226.

Cess, R. D. and Coauthors, 1996: Cloud feedback in atmospheric general circulation models: An update. *J. Geophys. Res.,* **101,** 12 791–12 794.

Colman, R. A., B. J. McAvaney, J. R. Fraser, and S. B. Power, 1994: Annual mean meridional energy transport modeled by a general circulation model for present and $2\times CO_2$ equilibrium climates. *Climate Dyn.,* **10,** 221–229.

Daniel, J. S., S. Solomon, and D. L. Albritton, 1995: On the evaluation of halocarbon radiative forcing and global warming potentials. *J. Geophys. Res.,* **100,** 1271–1285.

Eady, E. T., 1949: Long waves and cyclone waves. *Tellus,* **1,** 33–52.

Hansen, J., G. Russell, D. Rind, P. Stone, A. Lacis, S. Lebedeff, R. Ruedy, and L. Travis, 1983: Efficient three-dimensional global models for climate studies: Models I and II. *Mon. Wea. Rev.,* **111,** 609–662.

Held, I. M., 1993: Large-scale dynamics and global warming. *Bull. Amer. Meteor. Soc.,* **74,** 228–241.

——, and A. Y. Hou, 1980: Nonlinear axially symmetric circulations in a nearly inviscid atmosphere. *J. Atmos. Sci.,* **37,** 515–533.

Holton, J. R., 1979: *An Introduction to Dynamic Meteorology.* Academic Press, 319 pp.

Houghton, J. T., 1986: *The Physics of Atmospheres.* 2d ed. Cambridge University Press.

IPCC, 1990: *Climate Change, The IPCC Scientific Assessment,* WMO/UN Environment Programme. Cambridge University Press, 365 pp.

——, 1995: *Climate Change 1994. Radiative Forcing of Climate Change and an Evaluation of the IPCC IS92 Emission Scenarios.* Cambridge University Press, 339 pp.

Lacis, A., and J. Hansen, 1974: A parameterization for the absorption of solar radiation in the earth's atmosphere. *J. Atmos. Sci.,* **31,** 118–133.

——, and M. I. Mishchenko, 1995: Climate forcing, climate sensitivity, and climate response: A radiative modeling perspective on atmospheric aerosols. *Aerosol Forcing of Climate,* R. J. Charlson and J. Heintsenberg, Eds., Wiley and Sons, 440 pp.

——, D. Wuebbles, and J. Logan, 1990: Radiative forcing of climate by changes in the vertical distribution of ozone. *J. Geophys. Res.,* **95,** 9971–9981.

Logan, J. A., 1994: Trends in the vertical distribution of ozone: An analysis of ozonesonde data. *J. Geophys. Res.,* **99,** 25 553–25 585.

MacKay, R. M., and M. A. K. Khalil, 1995: $2\times CO_2$ experiments with the global change research center 2-D statistical dynamical climate model. *J. Geophys. Res.,* **100** (D10), 21 127–21 135.

McCormick, M. P., R. E. Veiga, and W. P. Chu, 1992: Stratospheric ozone profile and total ozone trends derived from the SAGE I and SAGE II data. *Geophys. Res. Lett.,* **19,** 269–272.

Molnar, G. I., and W. J. Gutowski Jr., 1995: The ''faint young Sun paradox'': Further exploration of the role dynamical heat-flux feedbacks in maintaining global climate stability. *J. Glaciol.,* **41,** 87–90

——, M. K. W. Ko, S. Zhou, and N.-D. Sze, 1994: Climate consequences of the observed ozone loss in the 1980's: Relevance to the greenhouse problem. *J. Geophys. Res.,* **99,** 25 755–25 760.

Peixoto, J. P., and A. H. Oort, 1992: *Physics of Climate.* Amer. Inst. Phys., 520 pp.

Peng, L., M.-D. Chou, and A. Arking, 1982: Climate studies with a multi-layer energy balance model. Part I: Model description and sensitivity to the solar constant. *J. Atmos. Sci,* **39,** 2639–2656.

——, ——, and ——, 1987: Climate warming due to increasing atmospheric CO_2: Simulations with a multilayer coupled atmosphere–ocean seasonal energy balance model. *J. Geophys. Res.,* **92,** 5505–5520.

Ramanathan, V., and R. E. Dickinson, 1979: The role of stratospheric ozone in the zonal and seasonal radiative energy balance of the earth–troposphere system. *J. Atmos. Sci.,* **36,** 1084–1104.

Ramaswamy, V., M. D. Schwarzkopf, and K. P. Shine, 1992: Radiative forcing of climate from halocarbon-induced global stratospheric ozone loss. *Nature,* **355,** 810–812.

Rennick, M. A., 1977: The parameterization of tropospheric lapse rates in terms of surface temperature. *J. Atmos. Sci.,* **34,** 854–862.

Schwarzkopf, M. D., and V. Ramaswamy, 1993. Radiative forcing due to ozone in the 1980s: Dependence on altitude of ozone change. *Geophys. Res. Lett.,* **20,** 205–208.

Shine, K. P., 1987: The middle atmosphere in the absence of dynamical heat fluxes, *Quart. J. Roy. Meteor. Soc.,* **113,** 603–633.

Stolarski, R. S., P. Bloomfield, R. D. McPeters, and J. R. Herman, 1991: Total ozone trends deduced from Nimbus 7 TOMS data, *Geophys. Res. Lett.,* **18,** 1015–1018.

Unauthenticated | Downloaded 10/21/21 05:38 AM UTC

Stone, P. H., 1974: The meridional variation of the eddy heat fluxes by baroclinic waves and their parameterization. *J. Atmos. Sci.,* **31,** 444–456.

——, and J. H. Carlson, 1979: Atmospheric lapse rate regimes and their parameterization. *J. Atmos. Sci.,* **36,** 415–423.

Trenberth, K. E., and A. Solomon, 1994: The global heat balance: Heat transports in the atmosphere and ocean. *Climate Dyn.,* **10,** 107–134.

Wang, W.-C., and N. D. Sze, 1980: Coupled effects of atmospheric N_2O and O_3 on the earth's climate. *Nature,* **286,** 589–590.

——, and P. B. Ryan, 1983: Overlapping effect of atmospheric H_2O, CO_2, and O_3 on the CO_2 radiative effect. *Tellus,* **35B,** 81–91.

——, G. Molnar, T. P. Mitchell, and P. H. Stone, 1984: Effects of dynamical heat fluxes on model climate sensitivity. *J. Geophys. Res.,* **89,** 4699–4711.

——, ——, M. K. W. Ko, S. Goldenberg, and N. D. Sze, 1990: Atmospheric trace gases and global climate: A seasonal model study. *Tellus,* **42B,** 149–161.

Washington, W. M., and G. A. Meehl, 1993: Greenhouse sensitivity experiments with penetrative cumulus convection and tropical cirrus albedo effects. *Climate Dyn.,* **8,** 211–223.

Watts, R. G., and M. Morantine, 1990: Rapid climatic changes and the deep ocean. *Climate Change,* **16,** 83–97.

Willmont, C. J., and D. R. Legates, 1993: A comparison of GCM-simulated and observed mean January and July surface air temperature. *J. Climate,* **6,** 274–291.

Unauthenticated | Downloaded 10/21/21 05:38 AM UTC